Dielectric properties of cubic boron nitride modulated by an ultrashort laser pulse

Xiaoshuang Kong,[1] Feng Wang,[1,*] Xiaoqin Zhang,[1,2] Zehui Liu,[1] and Xiaoli Wang[2]
[1]*School of Physics, Beijing Institute of Technology, Beijing 100081, China*
[2]*School of Mechanical Engineering, Beijing Institute of Technology, Beijing 100081, China*

(Received 1 June 2018; published 27 November 2018)

The transient dielectric responses of cubic boron nitride (cBN) modulated by an ultrashort laser pulse are introduced based on time-dependent density functional theory calculations. We theoretically investigate whether an ultrashort laser pulse is able to reversibly drive the electric and optical properties of cBN to change profoundly without damage. With easily tunable laser parameters, the cBN can even be switched by reversal of both elliptic and hyperbolic behaviors for a particular working frequency window. We describe the evolution of the transient dielectric function throughout the duration of the pulse, which can exhibit a reversible behavior driven by the instantaneous optical field for a purposely designed laser pulse, providing a fundamental possibility for applications of all-optical signal processing and optical-field-effect devices.

DOI: 10.1103/PhysRevA.98.053439

I. INTRODUCTION

The light-matter interaction has always been a topic of intensive research. Currently, precisely controlling the physical process of the interaction between ultrashort laser pulses and matter not only can obtain a new type of light field with a specific multidimensional spatiotemporal structure, but it also can acquire a new material state with specific physical properties. The few-cycle ultrashort laser pulses are characterized by ultrafast and flexible spatiotemporal wave form control, providing a powerful tool for developing new light field control physics and applications. An ultrastrong pulse makes laser-matter interactions a strongly nonlinear process. The ultrafast feature allows the pulse to control material properties nonthermally, coherently, and precisely, giving an observation of the ultrafast relaxation process in the microscopic regime on an unprecedented timescale. Apparently, the ability to drive and control transient material properties via an ultrashort laser pulse can open a number of interesting applications.

In the last decade, the interaction and modulation between ultrashort laser pulses and matter have received much attention in both theoretical and experimental fields. For instance, Durach *et al.* [1,2] introduced a quantum effect of metallization of diamond nanofilms induced by strong adiabatic electric fields, and then theoretically predicted an ultrafast dynamic metallization effect in a diamond nanofilm induced by an ultrafast ($\sim$1 fs) single-cycle optical pulse, which can be applied to creating a field-effect transistor. Apalkov *et al.* [3] theoretically predicted that an extremely intense and ultrashort pulse with a duration of several femtoseconds normally incident on a dielectric film could induce reversible and damage-free nonlinear optical responses, which puts forward the basic possibility of optical-field-effect devices with a bandwidth on the order of optical frequency. They also predicted a highly unusual and nontrivial behavior of metal nanofilms subjected to strong (intensity$\geqslant 5\times 10^{14}$ W/cm^2) ultrashort (near-single oscillation) optical pulse which induces a transition to a semimetal-like state, opening up the path of using metals as active elements for deep ultrafast modulation of optical fields [4]. Schiffrin *et al.* [5] have experimentally shown that a few-cycle optical wave form can increase the conductivity of fused silica by more than 18 orders of magnitude, less than 1 fs and free from breakdown, which allows the instantaneous field to reversibly switch on and off the electric current. Schultze *et al.* [6] have experimentally observed the reversible field-induced change of absorption, revealing the feasibility of manipulating the electronic structure and electric polarizability of a fused silica with a wave-form-controlled near-infrared few-cycle light field. Wachter *et al.* [7] theoretically investigated the generation of ultrafast currents in bulk α-SiO_2 induced by strong few-cycle laser pulses on the atomic scale based on time-dependent density functional theory (TDDFT), showing a reversible (sub)femtosecond-scale insulator-metal transition with the field-induced ac conductivity increased by more than 20 orders of magnitude. Kwon *et al.* [8] have experimentally and theoretically demonstrated that wide-band-gap insulators such as quartz, sapphire, and calcium fluoride undergo similar reversible semimetallization in a few-cycle strong optical field ($\sim$1 V/Å, 4 fs) within safety threshold, which potentially opens a door for the further development of electronic manipulation and signal processing. Kelardeh *et al.* [9] have investigated that an intense optical pulse of a few femtoseconds can deeply control the reversibility of the electron dynamics in buckled Dirac materials via changing the polarization and the propagation directions of the pulse. Lee *et al.* [10] have devised an asymmetric conduction to rectify the current by forming a heterojunction under the optical pumping by few-cycle laser pulses, promoting the development of electric signal manipulation of future light-wave electronics. Sommer *et al.* [11] experimentally accessed both the reversible and irreversible energy exchange between visible-infrared light and electrons of silica by timing the nonlinear polarization relative to the driving laser electric field with sub-30-attosecond

*wangfeng01@tsinghua.org.cn

accuracy. Overall, one conclusion that can be drawn from the above publications is that a strong ultrashort few-cycle laser pulse can drive interband electron dynamics and intraband electron dynamics in crystals, providing unique exciting opportunities for controlling transient changes in the electric and optical properties of a medium with unprecedented speed and accuracy without necessarily imposing physical damage.

Recently, Zhang *et al.* [12,13] have successfully manipulated dielectric properties, especially hyperbolic dispersion in diamond driven by ultrashort single-cycle laser pulses, using the TDDFT method, reflecting the depth-controllableness of ultrashort laser pulses on diamond and providing great potential for ultrashort device applications. Cubic boron nitride (cBN) with zinc-blende type structure, as a promising candidate material, has aroused increasing interest due to its unique advantages such as excellent physical hardness which is comparable to diamond, high thermal conductivity and high thermal stability, a low dielectric constant, and a large band gap. Consequently, it has a wide range of applications in modern microelectronic devices and can be used as a protective coating material [14]. It also has potential for high-temperature electronic devices [15]. What is particularly exciting here is, why do we not manipulate the dielectric properties of cBN? Considering the characteristics of ultrashort pulses, we wonder whether some new phenomena and new features will be expected. In this paper, using an *ab initio* approach based on TDDFT, we study the transient dielectric responses of cBN modulated by an ultrashort laser pulse.

The organization of the present paper is as follows. In Sec. II we introduce our methods to calculate the frequency-dependent dielectric function within the TDDFT framework. In Sec. III, we show calculated results of transient dielectric properties induced by the intense and ultrashort single laser pulse. Finally, the summary will be presented in Sec. IV.

II. METHOD

Our simulations in the present article are carried out with the OCTOPUS code (version 6.0) [16,17], which is a TDDFT calculation based on real time and real space. TDDFT have proven the practicality in calculating electron dynamics of finite systems, whereas it has also been proved to be applicable to infinite systems described by both density and current density [18,19]. The electron dynamics in a cubic unit cell of a crystalline solid under the influence of an electric field are solved via the following time-dependent Kohn-Sham (TDKS) equation in the velocity gauge (atomic units used unless stated otherwise),

$$i\hbar\frac{\partial}{\partial t}\psi_i(\mathbf{r},t) = h_{KS}(\mathbf{r},t)\psi_i(\mathbf{r},t), \tag{1}$$

where h_{KS} represents the time-dependent Kohn-Sham Hamiltonian defined by

$$h_{KS}(\mathbf{r},t) = \frac{1}{2m}\left[-i\hbar\nabla + \frac{e}{c}\mathbf{A}_{\text{eff}}(\mathbf{r},t)\right]^2 + V_{\text{eff}}(\mathbf{r},t), \tag{2}$$

m is the mass of an electron, e is an elementary charge ($e > 0$), and c denotes the scalar speed of light in vacuum. The time-dependent effective potentials are described as follows:

$$\mathbf{A}_{\text{eff}}(\mathbf{r},t) = \mathbf{A}_{\text{ext}}(\mathbf{r},t) + \mathbf{A}_{\text{ind}}(\mathbf{r},t),$$
$$V_{\text{eff}}(\mathbf{r},t) = V_{\text{ion}}(\mathbf{r},t) + \int d\mathbf{r}'\frac{\rho(\mathbf{r}',t)e^2}{|\mathbf{r}'-\mathbf{r}|} + V_{XC}(\mathbf{r},t), \tag{3}$$

where $\rho(\mathbf{r},t) = \sum_i |\psi_i(\mathbf{r},t)|^2$ is the valence electron density with the index i running over the occupied one-electron orbitals ψ_i. In the present calculation we freeze atomic positions, making them remain in the equilibrium position of the ground state. We only consider the dynamic of valence electrons, dealing with the interaction V_{ion} between valence electrons and the ionic core by the norm-conserving pseudopotential [20]. The exchange-correlation (XC) potential V_{XC} is employed to treat the electron-electron interactions in the adiabatic approximation. To model real crystalline solids in the presence of time-dependent electromagnetic fields using lattice periodic model systems, one has to deal with the special role of macroscopic polarization, as an independent degree of freedom [21] of the induced field $\mathbf{A}_{\text{ind}} = \mathbf{A}_{EM} + \mathbf{A}_{XC}$, which is the result of the reaction of the system to the external field $\mathbf{A}_{\text{ext}}$, where $\mathbf{A}_{EM}$ is the full electromagnetic potential, satisfying Maxwell's equation [22],

$$\left(\nabla^2 - \frac{1}{c^2}\frac{\partial^2}{\partial t^2}\right)\mathbf{A}_{EM} - \nabla\cdot(\nabla\cdot\mathbf{A}_{EM}) = -\frac{4\pi}{c}\mathbf{j}, \tag{4}$$

where $\mathbf{j}$ is the electric current density. All macroscopic components of the exchange-correlation contribution, which correspond to the macroscopic exchange-correlation field $\mathbf{A}_{XC}$, will not be taken into account in the present work. Note that here and in the rest of the paper, the vector potential is related to the electric field by $\mathbf{A}(t) = -c\int_{-\infty}^{t} dt'\mathbf{E}(t')$. Given that the scale of the cubic unit cell is usually much smaller than the wavelength of visible or infrared light and electron velocities are much smaller than the speed of light, we employ the dipole approximation and ignore the spatial dependence of the vector potential leading to

$$\frac{d^2\mathbf{A}_{EM}(t)}{dt^2} = 4\pi c\mathbf{j}(t), \tag{5}$$

where $\mathbf{j}(t)$ is an average electric current density over the unit cell volume Ω. The case of taking into account the surface charge effect, i.e., charging up of dielectric interfaces at finite distances, is known as the longitudinal geometry [23–26] approximation. A series of studies will be explored in the longitudinal geometry unless stated otherwise.

The transient dielectric function of excited cBN irradiated by laser pulses is similar to the numerical pump-probe experiments [27] that have been carried out, solving the TDKS equation in real time with pump and probe pulses. The pump single pulse with wave form [2] $\mathbf{E}_{\text{ext}}^{\text{pump}}(t) = \mathbf{E}_0 e^{-u^2}(1-2u^2)$ is employed to excite the electrons of the system, where $u \equiv t/\tau$, and $\mathbf{E}_0$ and τ are the amplitude and duration with the corresponding central frequency $\omega_l = 2\hbar/\tau$, respectively. The external probe pulse $\mathbf{E}_{\text{ext}}^{\text{probe}}(t)$ is applied to extracting dielectric properties of excited cBN. The dynamic dielectric function $\varepsilon(\omega)$ of frequency ω is defined as the ratio of the probe electric field $\mathbf{E}_{\text{ext}}^{\text{probe}}(\omega)$ to the effective electric field

$\mathbf{E}_{\rm eff}^{\rm probe}(\omega)$:

$$\mathbf{E}_{\rm ext}^{\rm probe}(\omega) = \varepsilon(\omega)\mathbf{E}_{\rm eff}^{\rm probe}(\omega), \tag{6}$$

where the $\mathbf{E}_{\rm eff}^{\rm probe}(\omega)$ is the sum of the external and induced electric field inside the substance under the polarization response. The $\varepsilon(\omega)$ can be represented as a Fourier transform of $\mathbf{E}_{\rm ext}^{\rm probe}(\omega)$ and $\mathbf{E}_{\rm eff}^{\rm probe}(\omega)$ at frequency ω: $\varepsilon(\omega) = \int dt e^{i\omega t}\mathbf{E}_{\rm ext}^{\rm probe}(t)/\int dt e^{i\omega t}\mathbf{E}_{\rm eff}^{\rm probe}(t)$. The diagonal elements of the dielectric function can be expressed in the following form:

$$\frac{1}{\varepsilon_{m,m}(\omega)} = 1 + \frac{\int dt e^{i\omega t}\frac{dA_{\rm ind,m}^{\rm probe}(t)}{dt}}{\int dt e^{i\omega t}\frac{dA_{\rm ext,m}^{\rm probe}(t)}{dt}}, \tag{7}$$

where subscript $m = x, y, z$ indicates the Cartesian component. Here we take a step function [23] as the external probe perturbation, $\mathbf{E}_{\rm ext}^{\rm probe}(t) = -(1/c)\mathbf{A}_0\delta(t - t_0)$. Finally, the dielectric function $\varepsilon_{mm}(\omega)$ of the system at a certain instant of time t_0 can be expressed as [13]

$$\frac{1}{\varepsilon_{m,m}(\omega)} = 1 + \frac{1}{A_{0,m}}\int_{t_0}^{T^{\rm probe}} dt e^{i\omega t - \gamma t}\frac{dA_{\rm ind,m}^{\rm probe}(t)}{dt}, \tag{8}$$

where γ is the damping factor. More detailed information about the TDDFT method can be found in Refs. [12,13].

In practical calculations, the TDKS equation is solved in real time and real space. The spatial grid used to represent the orbital wave function is discretized into 20^3 grid points with a spacing of each grid of 0.34 a.u. The k-point sampling is 8^3 in the first Brillouin zone. The real-time propagation is carried out by using an approximated enforced time-reversal-symmetry scheme [28] with a time step of 0.02 a.u.

III. RESULTS AND DISCUSSION

Figure 1(a) shows the crystal structure of cBN which is an isotropic indirect-gap insulator with a zinc-blende structure. The cubic unit cell used in our simulation contains four boron atoms and four nitrogen atoms with a lattice parameter a of 6.831 a.u. The band structure for cBN shown in Fig. 1(b) is calculated with ELK code (version 4.3.6) [29] using the PBE [30] XC potential. It can be seen that the overall profile is consistent with the available theoretical work. The indirect band gap is approximately 4.4 eV produced by the valence

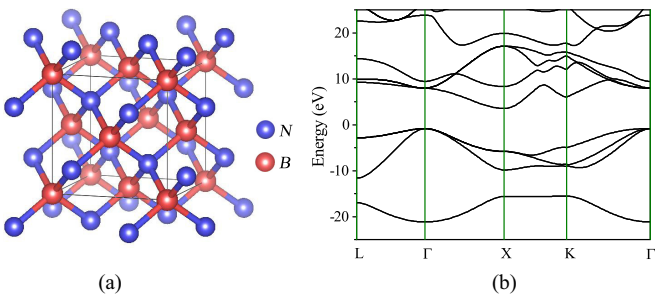

(a) (b)

FIG. 1. (a) The diagram of crystal structure in cBN, where the nitrogen atoms are represented by light blue balls and boron atoms are denoted by light red balls. (b) The band structure of cBN obtained via the ELK code.

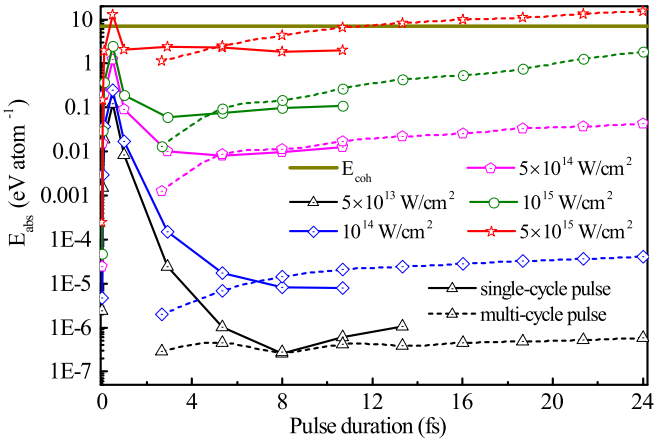

FIG. 2. The calculated energy absorption per atom in the cBN crystal as a function of the pulse duration, laser intensity, and pulse shape. Two pulse shapes are chosen: the single-cycle pulse mentioned above (solid lines and hollow symbols) and multicycle pulse expressed as $\mathbf{E}_{\rm ext}(t) = \mathbf{E}_0 \sin^2(\frac{\pi t}{T})\sin(\omega t)$ with a frequency of $\omega = 1.55$ eV (short dashed lines and hollow symbols).

band maximum at the Γ point and the conduction band minimum at the X point, which is smaller by about 2 eV with respect to the experimental measurement [31,32], but it is almost identical to the other calculations [33–36]. The underestimation of the band gap is mainly due to the fact that the simple form of the generalized gradient approximation [30] does not properly consider the self-energy of quasiparticles, making it insufficient to flexibly reproduce both XC energy and its charge derivative [36]. The corresponding calculated direct band gaps at the L, Γ, X, and K points are 12 eV, 8.8 eV, 9.3 eV, and 11 eV, respectively, which are larger than the indirect band gap.

In this paper, we expect to investigate the transient dielectric properties of cBN controlled via an ultrashort and ultrastrong laser pulse, with the aim of providing a potential possibility for applications of all-optical signal processing and optical-field-effect devices. What we are most interested in is the manipulation effect with the laser intensity range of 10^{13}–10^{15} W/cm^2 on a timescale of a few femtoseconds. Energy absorption is an inevitable and the most fundamental manifestation of the interaction of light with matter and a phenomenon of great technological relevance. One may wonder if such an ultrashort and ultrastrong control pulse may impose physical damage on cBN. Generally, the damage threshold is closely related to the pulse length and carrier frequency, and it can be judged by energy or critical density criteria [25,37]. Here we use the energy criterion to explain the impact of pulse duration and intensity on energy absorption of cBN as shown in Fig. 2. The absorption energy $E_{\rm abs}$ in the Ω is calculated by the difference between the electronic energy at time t and the ground-state energy in the simulation. Intuitively, it is also equivalent to the work done by the external field $\mathbf{E}_{\rm ext}(t)$, determined via $E_{\rm abs}(t) = \Omega\int_{-\infty}^{t}\mathbf{E}_{\rm ext}(t')\cdot\mathbf{j}(t')dt'$. The solid lines and hollow symbols represent the absorption energy as a function of the duration of a single pulse for an ultrashort timescale under different laser intensities. The short dashed lines and hollow symbols show the result induced by

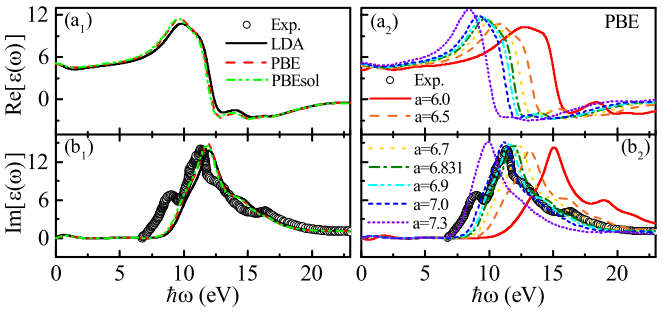

FIG. 3. The real (upper panels) and imaginary parts (lower panels) of the ground-state dielectric function of cBN calculated with various XC potentials (left panels) and different lattice parameters a ($a = 6.0$ a.u., 6.5 a.u., 6.7 a.u., 6.831 a.u., 6.9 a.u., 7.0 a.u., and 7.3 a.u.; right panels) taking the PBE XC potential as an example. The dark gray circles correspond to the imaginary part of the experimental data of Osaka *et al.* [41].

multicycle pulses for longer pulse duration expressed as $\mathbf{E}_{\text{ext}}(t) = \mathbf{E}_0 \sin^2(\frac{\pi t}{T}) \sin(\omega t)$ with a frequency of $\omega = 1.55$ eV. The calculated cohesive energy of cBN obtained by the PBE [30] XC potential is about 6.94 eV per atom given by a thick dark yellow solid line which agrees well with the experimental data of 6.68 eV per atom [38]. Observing the overall information in Fig. 2, the absorbed energy of cBN increases with an increase of laser intensity. The energy absorption at pulse duration of 0.5 fs induced with a single-cycle laser pulse and over 12 fs irradiated by a multicycle pulse has exceeded the cohesive energy line when $I = 5\times10^{15}$ W/cm^2. During the short pulse duration segment of 0.5–8 fs, the damage threshold increases as the pulse duration increases. In the long pulse duration of more than 8 fs, the damage threshold decreases because of the importance of electron-electron scattering at longer time. Figure 2 elucidates that, with proper parameter selection, an ultrashort optical single pulse with a peak intensity $\leqslant 5\times10^{15}$ W/cm^2 does indeed give rise to a transient field that is strong enough to make properties of the material drastically different from its equilibrium counterparts without imposing physical damage.

Moreover, it should be mentioned that our estimated damage threshold can be considered as the maximum intensity at which the material can be exposed without any damage, because during the simulation, we have used the default that the absorption energy of the conduction band electrons is completely transferred to the lattice. However, in reality, some of the energy may be lost so that the damage threshold will be pushed up [37]. Currently, it has been possible experimentally to obtain a single-cycle pulse with a width of 80 attoseconds [39]. The laser pulse length used in this article is 2.9 fs or 4.35 fs. Generally, there are two benefits to using an ultrashort pulse to phase-coherently control the dielectric properties of a material: (1) The detrimental scattering does not occur on such a short timescale, which typically occurs on the order of ~100 fs [40]. (2) The energy of the ultrashort laser pulse was concentrated in a very short time interval; a strong transient field generated by that is enough to make the properties of the material change significantly, making them drastically different from their equilibrium counterparts and causing no physical damage.

Figure 3 depicts both real and imaginary parts of dielectric functions calculated with various XC potentials and lattice parameters in the field-free case, where the curve in the bottom panel highlighted with the dark gray circles is the experimental data of Osaka *et al.* obtained from the reflectance spectrum by the Kramers-Kronig transformation. In our calculation, we take the time period $T^{\text{probe}} - t_0$ as 200 a.u. with the aim to ensure a sufficient resolution of the spectrum obtained by the Fourier transform. $\gamma = 0.02$ is chosen for a smearing parameter to simulate finite-lifetime effects of the excitations and to remove a spurious divergence which appears at low energy [42].

In analogy to the static density functional theory (SDFT), TDDFT is also in principle exact, but in practice one needs approximations for the accurate time-dependent XC potential with nonlocality in space and time, and the property of derivative discontinuity. So far, the popular applications of TDDFT have almost taken no account of the discontinuities, and exclusively relied on the adiabatic approximation which feeds the instantaneous time-dependent density into a known static XC potential of SDFT. However, it is unclear whether the progression towards a more accurate XC potential in SDFT necessarily correlates with an improved description in TDDFT. Therefore, many benchmark studies have explored the performance of using the static XC potential within the adiabatic approximation for the calculation of TDDFT. The scope of the previous benchmark studies has been primarily limited to the regime of the linear and the perturbative response, where TDDFT is an effectively standard time-dependent perturbation theory. There are very few benchmarks considering the regime of the nonlinear and the nonperturbative response in a strong-excitation process where TDDFT is a computationally attractive approach. For the case of describing the interaction of an intense laser and dielectric using TDDFT, as the laser intensity increases, the discrepancy between the different time-dependent XC potentials can be inferred to gradually fade away. This is because the peak laser intensities are comparable to the static electric field experienced by an electron in its own molecular orbital [43], and obviously larger than the XC potential associated with the electron-electron interaction. Thus for higher intensities the XC potential becomes less and less important due to the strongly dominant external field [44]. We do not expect quantitative agreement between the model and experiment. For this we would need to use the correct time-dependent XC potential and the correct atomic pseudopotentials with correct bound and excited states. Our aim is to illuminate the underlying concept of controlling the transient dielectric responses of cBN by controlled ultrashort laser pulses and to explore a wider range of laser parameters that would be relevant to more interesting manipulation.

In the left panel of Fig. 3, we compare the influence of three typical XC potentials (LDA [45], PBE [30], and PBEsol [46]) on the dielectric function. Our calculations are in agreement with experimental results as a whole but there is a little deviation between them. We can validate from Fig. 3(b_1) in left panel that the imaginary part of dielectric function appears as an obvious blueshift in comparison to the experimental data. The measured data show major peaks at 11 eV and 8.9 eV, while the calculated peak position is at about 12 eV nearly without the second major peak at the lower frequency.

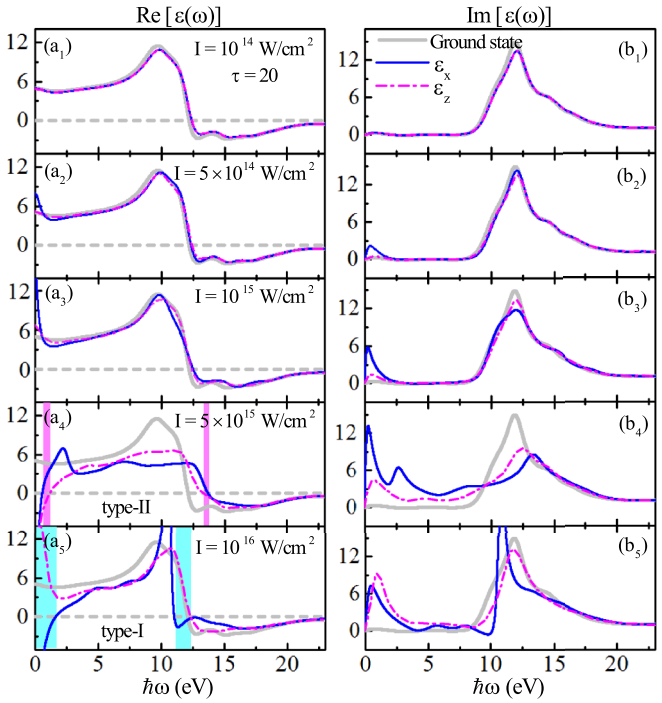

FIG. 4. The transient calculated dielectric functions of cBN induced by single-cycle laser pulse with varying intensity and frequency $\omega_l = 2.72$ eV. The blue solid or magenta dash-dotted line indicates the result of probing with the direction parallel or perpendicular to the single-cycle pump laser polarization direction (along the x axis), respectively, after the pump ends. The thick gray solid line expresses the dielectric function in the ground state. The horizontal gray dashed lines in the real-part panels indicate $\mathrm{Re}[\varepsilon(\omega)] = 0$. The frequency window for type-I [$\varepsilon_\perp$ (ε_{xx}) < 0, $\varepsilon_\parallel$ (ε_{zz}) > 0] hyperbolic dispersion is marked by a light-blue shaded (light gray) area, and the frequency window for type-II [$\varepsilon_\perp$ (ε_{zz}) < 0, $\varepsilon_\parallel$ (ε_{xx}) > 0] hyperbolic dispersion is represented by a magenta-shaded (dark gray) region.

The slight deviation may be due to the difference in lattice parameter. In general, there are two schemes for choosing the lattice parameter in theoretical simulations: the experimental values at room temperature and the equilibrium values of theoretical calculations at zero temperature. In this paper, we take the experimental lattice parameter [47] determined by x-ray diffraction at zero pressure. The curves in the right panel show the lattice parameter dependence of the dielectric function variation taken with a fixed PBE XC potential, where the olive green dash-dotted line represents the result calculated with the experimental lattice parameter. It is found that the lattice parameter does play a non-negligible role in adjusting the absorption peak position. With the increase of the lattice parameter, the peak position appears with a palpable redshift. However, what is gratifying is that the calculated peak values are very close to the measured one. In conclusion, PBE obtains a very good compromise between computational ease and accuracy; thus it will be used in our subsequent calculations.

Next, we show the transient dielectric properties of cBN with an emphasis on the nonlinear response regime. One set of trajectories calculated for transient dielectric functions at different intensity levels is depicted in Fig. 4, which is probed at a time when the pump pulse is over. Here, the ultrashort single pulse is pumped along the x axis with frequency of $\omega_l = 2.72$ eV ($\tau = 20$ a.u.) and pulse length of 6τ. In the figure, the blue solid and magenta dash-dotted lines indicate the dielectric functions with the polarization direction of the probe field along the x axis (ε_{xx}) and the z axis (ε_{zz}), respectively. For convenient comparison, the ground-state dielectric function emphasized with the thick gray solid line is added in each panel. First, we take the case of ε_{xx} for detailed analysis. At relatively low laser intensity ($I = 10^{14}$ W/cm^2), as evident from Figs. 4(a$_1$) and 4(b$_1$), the global shape of the spectrum is not much changed with respect to the ground-state calculation. But it is not to be ignored that the absorption peak located around 12 eV is slightly lower than that of the ground state, which is feature of a perturbative excitation process. When the incident intensity increases to $I = 10^{15}$ W/cm^2, it is observed that the oscillation around the low frequency (below 5 eV) is becoming more remarkable in both real and imaginary parts, implying the existence of classical metallization behavior [2,48,49] which resembles the plasmonic metal in the optical characteristics. Furthermore, as the intensity of the laser field increases gradually ($I > 10^{15}$ W/cm^2), the dielectric properties have undergone substantial changes, as can be seen from Figs. 4(a$_4$)–4(b$_5$). The spectra exhibit strong oscillations in the low-frequency region and the absorption peak value decreases in contrast with the field-free case, signifying that the electronic states are highly nonequilibrium. Generally speaking, the apparently enhanced dynamic metallization is due to the mutual influence of both the adiabatic and diabatic mechanisms [2]. The adiabatic mechanism determines the change of the band structure by the influences of strong fields of the laser on electron states in dielectrics, while the diabatic mechanism determines the interband and intraband transitions through the laser-induced coherence of the dielectric states which leads to quantum interference between the excitation pathways that control the optical response. The nonlinear process of ultrafast and dissipative insulator-metal transition on the (sub)femtosecond scale indicates that the transient dielectric properties of the dielectric are strongly influenced by the excitation dynamics.

With the intensity of the applied laser field increasing, the electron-hole pairs excited by perturbative and tunneling mechanisms increase slowly, accompanying a multiphoton energy absorption. The laser-excited carriers affect the dielectric function by band filling, free carrier response, and changes in the band structure due to ionic screening and other many-body effects [50]. A strong electric field narrows the band gap so that electrons are more easily excited to the conduction band. However, once the laser field is strong enough to tunnel between neighboring atoms according to the Keldysh parameters in the strong-field ionization model [51], the obvious nonlinear response will be occurred. A strong laser field near the damage threshold results in high-density electron-hole pairs at the dielectric surface, and plasma behavior dominates at higher laser intensities, resulting in optical properties that follow the properties of the plasma medium. The plasmon oscillation frequency ω_p is given by $\omega_p = \sqrt{\rho e^2/m_e\varepsilon_0}$ [12], where ρ is the electron density and ε_0 is the permittivity of a vacuum.

One more interesting feature here is found by comparing the transient dielectric functions ε_{xx} and ε_{zz} that probe after

the pump ends. At the lowest intensity $I = 10^{14}$ W/cm^2, the spectra of ε_{xx} and ε_{zz} do not change much in shape, which means that cBN is still an isotropic material after the weak laser irradiation. However, for the cases of stronger laser field $I > 10^{15}$ W/cm^2, ε_{xx} and ε_{zz} feature strong anisotropy [52], indicating that the electron states are highly unbalanced after exposure to intense radiation. The generation of the anisotropic behavior is caused by the asymmetric conduction band electron population generated by the pump laser field, as occurs in silicon experiments [53]. When $I \geqslant 5\times10^{15}$ W/cm^2, we also note that the dielectric functions ε_{xx} and ε_{zz} in real part show opposite signs, showing that the excited cBN has become a hyperbolic-like material in nature. The regions in the real part of the frequency window $\varepsilon_{xx} < 0$, $\varepsilon_{zz} > 0$ marked with a light blue shadow (light gray area) and the frequency window $\varepsilon_{xx} > 0$, $\varepsilon_{zz} < 0$ denoted by a magenta shadow (dark gray area) as shown in Figs. 4(a_4) and 4(a_5) represent two different types of hyperbolic dispersion. Refraction is one of the main theoretical foundations of optical device design. Especially the discovery of negative refraction [54] and the proposal of its theory have greatly enriched the existing basic optical theory and applications [55–58]. Generally speaking, the realization of the negative refraction of ultrashort-wavelength electromagnetic waves is critical to the development of nanoscale electromagnetic wave control technology.

A hyperbolic metamaterial [59,60], a most unusual type of electromagnetic metamaterial that is very interesting, is an artificial anisotropic medium with unique properties that exhibits hyperbolic dispersion. It refers to the materials in which the principal component of the permittivity tensors has opposite sign to the other two components. This feature of hyperbolic materials determines their unique applications. Placing a single-photon emitter based on nanodiamonds on the surface of hyperbolic metamaterials can dramatically increase the generation of single photons [61], which facilitates the development of quantum computers and quantum communication technology equipment. Threshold-less Cherenkov radiation can be realized in hyperbolic metamaterials [62], which plays an important role in the study of interaction of flying electrons with nanostructures on a chip. And the successful manipulation of transient hyperbolic dispersion provides great potential for applying the concept of light control, which can be used to modulate the dielectric function of optical medium of the signal light with another light beam.

As evident in Fig. 5(b), a transverse magnetic (TM) polarized (p-polarized) light with the Poynting vector of S_i is incident to cBN from air along the direction of the pump pulse (x axis). Let the incident plane be the air/cBN interface at $x = 0$ (yz plane). Air (cBN) occupies the region of $x > 0$ ($x < 0$). The incident angle is θ_i and the optical axis is parallel to the x axis. The real components of dielectric function ε_{xx} and ε_{zz} with opposite signs give the type of equifrequency contour (EFC) in the wave vector plane a hyperbola in Fig. 5(a), characterized by the hyperbolic dispersion relation $k_\parallel^2/\varepsilon_\perp^R + k_\perp^2/\varepsilon_\parallel^R = \omega^2/c^2$ [13], where $\varepsilon_\parallel^R$ or $\varepsilon_\perp^R$ represents the real part of the dielectric function that probed parallel or perpendicular to the air/cBN interface; c is the light speed in the vacuum. For EFC schematic as denoted in Fig. 5(a), the red circle denotes the EFC in air which

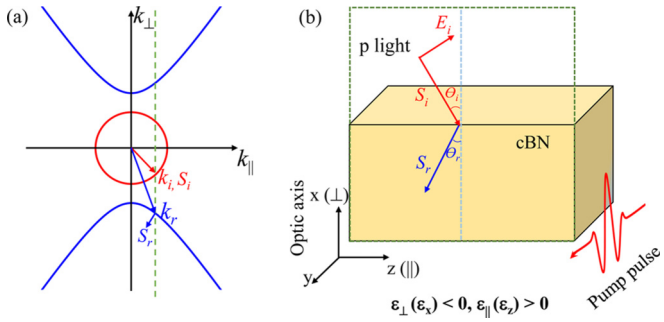

FIG. 5. (a) The EFC of cBN (the blue hyperbolas), as well as the EFC of air (the red circle), which follows from the hyperbolic dispersion relation, illustrating the case of $\varepsilon_\perp^R$ (ε_{xx}) < 0, $\varepsilon_\parallel^R$ (ε_{zz}) > 0. k_i (k_r) and S_i (S_r) are the incident (refractive) wave vector and Poynting vector, respectively. (b) Schematic of negative refraction that occurs when TM p-polarized light is incident from air onto excited cBN. The pulse is pumped along the optical axis (the x axis).

is an isotropic medium and the blue hyperbola is the EFC in excited cBN. The Poynting vector S_i in air is incident along the direction of wave vector k_i. Their components parallel to the interface are always consistent with the parallel component of wave vector k_r during refraction. Compared with k_i, S_i, and k_r, the Poynting vector S_r in the hyperbolic material during refraction is always on the opposite side of the interface normal, accompanying the negative refraction angle θ_r illustrated in Fig. 5(b). Interestingly, in detail, there are two hyperbolic behaviors, referring to type I for $\varepsilon_\perp^R(\varepsilon_{xx}) < 0$, $\varepsilon_\parallel^R(\varepsilon_{zz}) > 0$ and type II for $\varepsilon_\perp^R(\varepsilon_{zz}) < 0$, $\varepsilon_\parallel^R(\varepsilon_{xx}) > 0$. In general, the type-I hyperbolic material has a lower reflectivity, and the high-resolution imaging is better than the type II [63].

The transient dielectric properties manipulated at certain time points by a laser field with the parameters frequency $\omega_l = 1.8$ eV ($\tau = 30$ a.u.), pulse duration 6τ, and different peak laser intensities are displayed in Figs. 6 and 7 to further verify the feasibility to control strong anisotropy of cBN by laser technology. Surprisingly, for $I = 10^{14}$ W/cm^2 and $I = 5\times10^{14}$ W/cm^2, the metal-like and hyperbolic behaviors of the cBN dielectric functions were observed during the duration of single pulse. Here, we take time points of T_{p1}, T_{p2}, and T_m during the pulse, which are indicated with gray vertical dashed lines in Fig. 6(a) to analyze the transient dielectric response. As observed in Fig. 6(b), when $I = 10^{14}$ W/cm^2, the instantaneous dielectric functions at T_{p1} and T_{p2} appear greatly anisotropic, especially the hyperbolic response of type I. The widest hyperbolic dispersion range at T_{p2} is from 4.16 eV to 6.21 eV which exceeds the hyperbolic window of graphite (4.4–5.17 eV) [64], MgB_2 (2.59–3.72 eV) [64], and CaN_2 (0.38–1.4 eV) [65]. Instead, the instantaneous dielectric functions ε_{xx} and ε_{zz} of excited cBN at T_m and at the end of the pulse T_l coincide with the results of ground state. It is confirmed that the excited cBN could return to its original state when the time of vector potential $\mathbf{A}(t)$ or induced electric current density $j(t)$ is zero, which indicates the possibility of reversible and damage-free manipulating of dielectric properties of dielectrics by shaped pulse. Due to the

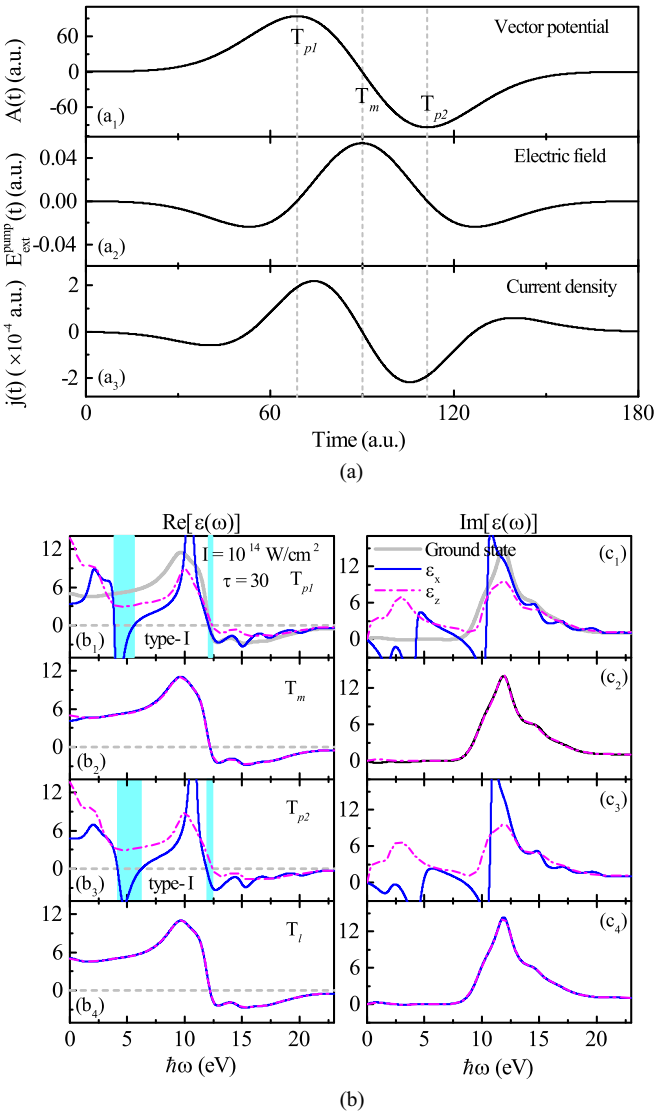

FIG. 6. (a) The vector potential (a_1) and its corresponding external laser field (a_2) and induced current density (a_3) with $\omega_l = 1.8$ eV ($\tau = 30$ a.u.) and $I = 10^{14}$ W/cm^2. The vertical light gray dashed lines mark three special time points of the vector potential: peak time $T_{p1} = 68.78$ a.u., $T_{p2} = 111.22$ a.u., and middle time $T_m = 90$ a.u. (b) The calculated dielectric functions of excited cBN probed with the direction either parallel (ε_{xx}, blue solid line) or perpendicular (ε_{zz}, magenta dash-dotted line) to the pump polarization direction at certain time during the pump pulse corresponding to the time points marked in panel (a).

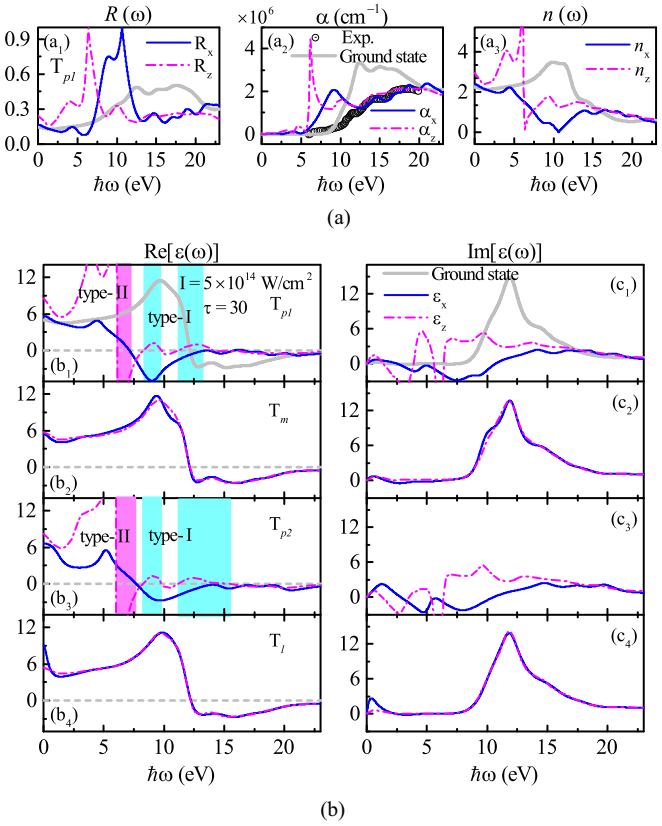

FIG. 7. (a) The reflectivity (a_1), absorption coefficient (a_2), and refractive index (a_3) spectra of cBN at ground state (light gray solid line) and at excited state induced by a single pulse with a frequency of $\omega_l = 1.8$ eV ($\tau = 30$ a.u.) and intensity $I = 5\times10^{14}$ W/cm^2 at time point T_{p1} corresponding to (b_1) and (c_1). The ground-state spectra are added in each panel with gray solid line and the dark gray circles show the experimental measurements [66]. (b) The dielectric functions similar to those of Fig. 6(b) but with the intensity $I = 5\times10^{14}$ W/cm^2.

large bandwidth of attosecond laser pulses, it is possible to make the interference between more different quantum pathways, providing exciting opportunities for coherent control of electron motion in solids with unprecedented speed and accuracy.

For the simulations of stronger laser intensity $I = 5\times10^{14}$ W/cm^2 presented in Fig. 7, both types of hyperbolic behaviors appear at T_{p1} and T_{p2} with wide working frequency windows. The working windows of both type I and type II at T_{p2} are wider than at T_{p1}. Even the widest type-I hyperbolic dispersion window reached 4.29 eV (11.16–15.45 eV) at T_{p2} plotted in Fig. 7(b_3). These unexpected discoveries offer a wide range of possibilities for further manipulating the hyperbolic responses during pump pulses by easily tunable laser parameters.

However, the imaginary part of dielectric functions probed at T_{p1} and T_{p2} are lower and the positions of the absorption peaks are ambiguous overall, as seen in Figs. 7(c_1) and 7(c_3). The small, even negative, contributions in the imaginary part of the dielectric function imply that the anisotropic response is induced, which results from the optical emission caused by the decrease of the lower-energy electron-hole and the increase of higher-energy electron-hole [52]. For further exploration, the reflectivity $R(\omega)$, absorption coefficient $\alpha(\omega)$, and refractive index $n(\omega)$ of cBN at normal incidence on the yz plane (denoted with the blue solid line) and xy plane (denoted with the magenta dash-dotted line) that probed at the T_{p1} time point are exhibited in Fig. 7(a). Their calculation details will be described later. For comparison, the calculated ground-state results are added in each panel with the light gray solid line. The excited-state results between about 11–20 eV are lower than those in the ground state. The dark gray circles denote the experimental absorption coefficient [66], which shows a

slow rise above 6 eV followed by a steeper one above 10 eV, with three prominent structures situated at about 11.5, 14, and above 17 eV. In theory the ground state yields peaks at 12.4, 15, and 16.7 eV. This good agreement is only obtained when the electron-hole interaction is included [67]. Taking ε_{xx} at T_{p1} for detailed analysis, we can see from Figs. 7(a_1) and 7(a_2) that in the low-frequency region (below 5 eV), nearly zero R_x and α_x imply that the excited cBN has been induced into a transparent one. The high R_x and α_x in the region of 7–11 eV are higher than the results in the ground state. Especially a total reflection appears in the reflectivity spectra around 10.6 eV, which is the manifestation of metal-like behavior.

As an illustration, Fig. 7(a_3) shows the $n(\omega)$ derived from dielectric function by $n(\omega) = \sqrt{[\varepsilon^R(\omega) + |\varepsilon(\omega)|]/2}$, where $\varepsilon^R(\omega)$ represents the real part of dielectric function. The profile of the $n(\omega)$ is similar to the trend of the real part of the dielectric function. The change of refractive index Δn between n_x (or n_z) and $\bar{n}$ is closely related to signal manipulation [11]. Thus, we defined an average refractive index $\bar{n}(\omega)$ in the range of 7–11 eV with the ground-state data, which is equal to 3.1. The relative refractive index change $\Delta n/\bar{n}$ of cBN can reach 100% at 10.6 eV. The fascinating finding promotes the possibility of the operation of a dielectric switch/modulator at 100 THz or beyond [11].

It is demonstrated that an isotropic material may be made hyperbolic-like one by a tunable laser pulse. The hyperbolic property can be adjusted into different operating frequency regions in the electromagnetic spectrum from the infrared to the ultraviolet frequencies. In addition, combined with Fig. 4, it has been proven that controlling the dielectric properties of the cBN at the end of the pulse to achieve hyperbolic dispersion requires stronger single-cycle pump pulses. But that may cause the material to absorb excessive energy as displayed in Fig. 2 and be destroyed.

As cBN is being excited to exhibit strong anisotropy, the appearance of isoindex points ($n_\parallel = n_\perp$) has attracted our attention. $n_\parallel$ or $n_\perp$ denotes the real part of the refractive index for dispersion branches. At these isoindex energy points, the excited anisotropic cBN appears isotropic and the plane wave in any direction experiences the same phase delay. Narrow bandwidth filters ($\Delta\lambda < 0.1$ nm) can be fabricated based on this fascinating feature, which may ideally have potential applications in optical communication between moving objects [68]. Its performance depends crucially on a superior figure of merit (FOM) at the isoindex point λ_0. The FOM is defined by $|d(\Delta n)/d\lambda|/\lambda_0$, where $\Delta n = n_\parallel - n_\perp$ [68,69]. From Table I, it can be seen that the excited cBN at time T_p pumped by single-cycle pulse laser with slightly higher intensity $I = 5\times10^{14}$ W/cm^2 has extremely large values of dispersion $[d(\Delta n)/d\lambda]$ at the isoindex energy points. The result further confirms that the stronger laser pulse will produce more complex and interesting dielectric response. Excitingly, the superior FOM of cBN is much higher than that of Bi_2Se_3 and Bi_2Te_3, which are considered good candidates for thinner or narrower wavelength filters.

In the following, we discuss the impact of free relaxation time between pump and probe field on the frequency-dependent dielectric function probed at the time the pump is switched off. Taking the case of ε_{xx} at $\omega = \omega_l = 2.72$ eV and $I = 10^{15}$ W/cm^2 as an example is shown in Fig. 8(a). We extract the dielectric functions with a free relaxation time of one duration of the single-cycle laser pulse (0–6τ). The small peak at the low-frequency region and the main absorption peak of the dielectric function can change orderly with the extension of free relaxation time, which due to the electron-hole excitation and energy deposition occur and come to an equilibrium. Furthermore, a distinctive feature is observed: the imaginary part of dielectric function shows negative behaviors in the low-frequency region (below 2.5 eV) at a certain free relaxation time. Next, we present the free relaxation time-dependent imaginary part of the dielectric function at $\omega_l = 2.72$ eV in Fig. 8(b). For obtaining intuitional results, we select a sufficiently long time range as the free

TABLE I. Figure of merit for excited cBN at the isoindex points ($n_\parallel = n_\perp$) and other isoindex filter materials [68,69].

Material	Intensity (W/cm^2)	Time points	Energy (eV)	FOM (μm^{-2})
cBN	1×10^{14}	T_{p1}	3	5.3
			4	335
			9.7	763.1
		T_{p2}	10.1	1650.1
	5×10^{14}	T_{p1}	6.3	3689.8
			7.4	234.6
		T_{p2}	6.2	3158.4
			7.6	229.1
Bi_2Se_3 [68]			1.06	35
Bi_2Te_3 [68]			2.32	10
CdS [69]			2.36	2.3

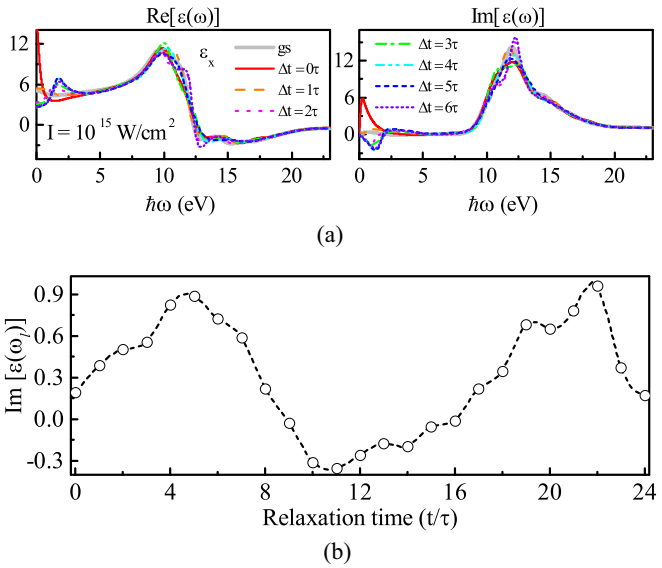

FIG. 8. (a) The frequency-dependent dielectric function ε_{xx} of cBN affected by the free relaxation time, which was induced by single-cycle pulse with peak laser intensity of 10^{15} W/cm^2, laser frequency of 2.72 eV. (b) The imaginary part of dielectric function at $\omega = \omega_l = 2.72$ eV as a function of free relaxation time extended from 0 to 24τ.

relaxation time. This demonstrates that the absorption results at $\omega_l = 2.72$ eV depend mostly on the relaxation time and oscillate periodically due to interferences between the occupied states involved. Interestingly, the oscillation period is about twice the length of the pump pulse. The system can serve as a thermalized electron-hole plasma with fixed numbers of electrons and holes. The time dependence of a dielectric function is therefore a clear sign of a nonstationary state, i.e., a linear combination of nondegenerate eigenstates. This proves that the dielectric function can be adjusted by controlling the length of free relaxation time between pump and probe field.

The adiabatic metallization predicted theoretically may be supported by the observation of the optical-field-induced transient reflectivity. The Fresnel reflection coefficient $R(\omega)$, which can be feasibly measured experimentally for studying the response to the excitation, of two different types of polarized light at the incident angle θ_i is defined by [70]

$$R(\omega) = \begin{cases} \left|\frac{\sin(\theta_i-\theta_{t1})}{\sin(\theta_i+\theta_{t1})}\right|^2, & s \text{ polarized}, \\ \left|\frac{\varepsilon_\parallel \tan\theta_{t2}-\tan\theta_i}{\varepsilon_\parallel \tan\theta_{t2}+\tan\theta_i}\right|^2, & p \text{ polarized}, \end{cases} \tag{9}$$

where θ_{t1} and θ_{t2} can be expressed as $\sin\theta_{t1} = \sin\theta_i/\sqrt{\varepsilon_\parallel}$ and $\tan\theta_{t2} = \sqrt{(\varepsilon_\perp \sin^2\theta_i)/(\varepsilon_\parallel\varepsilon_\perp - \varepsilon_\parallel \sin^2\theta_i)}$, respectively. The refraction angle θ_r of the Poynting vector S_r can be obtained by $\theta_r = (\sqrt{\varepsilon_\parallel}\theta_i)/(\varepsilon_\perp\sqrt{1-(\sin^2\theta_i/\varepsilon_\perp)})$. Clearly, for $\varepsilon_\parallel > 0$ and $\varepsilon_\perp < 0$, the θ_r and θ_i are of opposite signs implying a negative refraction.

For the case of normal incidence, $R(\omega)$ is reduced to $R(\omega) = |(\sqrt{\varepsilon_\parallel}-1)/(\sqrt{\varepsilon_\parallel}+1)|^2$. The absorption coefficient $\alpha(\omega)$ can be obtained by $\alpha(\omega) = 2\omega\kappa(\omega)/c$, where $\kappa(\omega)$ is the extinction coefficient which can be derived from $\varepsilon(\omega)$: $\kappa(\omega) = \sqrt{(|\varepsilon_\parallel| - \varepsilon_\parallel^R)/2}$. The absorption coefficient of the calculated ground state result and the experimental data are plotted in Fig. 7(a$_2$). Figure 9 displays the reflectivity $R(\omega)$ of cBN at normal incidence on the yz plane (R_x) and the xy plane (R_z) both with and without the contribution of a single pulse in comparison with the experimental measurement of cBN that sinter synthesized under high pressure and temperature [41], where the light gray solid line in each panel is the calculated reflectivity without laser action. Overall, the shapes of the calculated curves are very similar to the experimental curve, with three peaks between 10–20 eV. For easy comparison, we moved the experimental curve downward to coincide with the broad peak of the ground-state reflection curve at around 17 eV. When the laser intensity $I < 5\times10^{14}$ W/cm^2, the calculated result agrees well with that in the ground state which is close to the experimental spectrum. Unsurprisingly, R_x and R_z are also completely coincident with each other. With the increase of laser intensity, the complicated physical behavior appears: There is a distinct oscillation with different amplitudes displayed at the low-energy region. Particularly, when $I \geqslant 5\times10^{15}$ W/cm^2 as shown in Fig. 9(a$_4$), the total reflection appears at the low-frequency region in both R_x and R_z, echoing the metallization behavior. And the reflectivity in region 5–18 eV is smaller than that at the ground state. By comparing the R_x and R_z of excited cBN, it can be seen that the isotropic cBN could be induced into an anisotropic dielectric. The strong laser field near the damage threshold

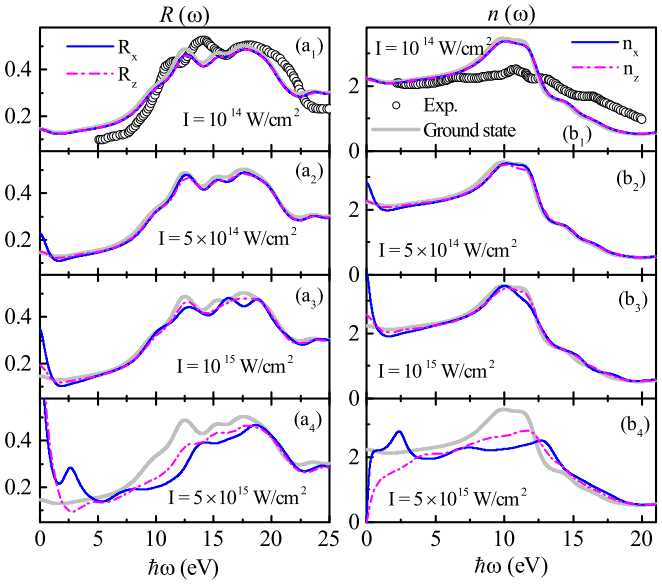

FIG. 9. The reflectivity spectrum (left panel) and refractive index (right panel) of cBN at an excited state induced by single pulse with the frequency of $\omega_l = 2.72$ eV and at ground state (thick light gray solid line) at normal incidence on the yz plane (blue solid line) and xy plane (magenta dash-dotted line). The black circles denote the experimental measurement [41,66].

produces high-density electron hole pairs on the dielectric surface. At higher laser intensity, the plasma behavior dominates, leading to the change of optical properties with the properties of plasma medium and strong reflection. We also depict the $n(\omega)$ of cBN after the pump field switched off with different peak intensities, as shown in the right panel of Fig. 9. The experimental data of the refractive index marked with black circles were obtained by Miyata and co-workers from their measured reflectance and transmittance data [66]. With the rise of the laser energy, the change of the refractive index between excited state and ground state in cBN is remarkable. And the anisotropic property appears with the pulse intensity increasing just similar to the reflectivity section.

All of the above results about manipulating the optical properties are based on the simulation of the longitudinal geometry approximation, which can be seen as an isolated system. There is another macroscopic geometry in the simulation to mimic the presence of metallic contacts not explicitly treated, $\mathbf{A}_{\text{eff}}(t) = \mathbf{A}_{\text{ext}}(t)$, namely transverse geometry [7,26,27]. It amounts to adding a metal electrode on both ends of the material as in the schematic view in Fig. 10 and can be described as follows: an intense single pulse polarized parallel to the electrodes, along coordinate x, to drive the generated carriers towards the electrodes. The net charge of opposite sign at the opposite facets of the dielectric has been accumulated, and further transferred to the electrodes, and then canceled through the metal leads in the ideal case.

Finally, we show the electric current density $j(t)$ and electric conductivity $\sigma(\omega)$ of cBN calculated within two geometries in Fig. 11. The $j(t)$ as a function of the pulse duration for different laser intensities is displayed in Fig. 11(a). In the longitudinal geometry, when the laser intensity

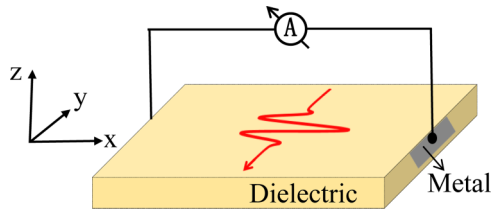

FIG. 10. A schematic representation of laser pumping dielectric in the transverse geometry. Two metal electrodes are respectively added on both ends of the material, and are connected to the ammeter by wires.

$I < 10^{15}$ W/cm^2, the $j(t)$ resembles closely the laser shape represented by the light gray solid line and the phase lag of approximately $\pi/2$ between them indicates a nondissipative response process. The field-induced polarization current density $j(t)$ was gentle until $I = 10^{15}$ W/cm^2; only a slight oscillation occurs on the field trailing edge because of the emergence of excitation states.

By contrast with the left panel in Fig. 11(a), the electron dynamics in the transverse geometry is more sensitive to the laser than that in the longitudinal geometry. For the same intensity, the trend of the current density curve in the transverse geometry is bumpier. And the similar low-amplitude coherent oscillations on the field trailing edge begin occurring at the laser intensity $I = 10^{13}$ W/cm^2, which is nearly two orders of magnitude lower than that in the case of longitudinal geometry. This is owing to the influences of induced vector potential $\mathbf{A}_{\rm ind}(t)$ and external vector potential $\mathbf{A}_{\rm ext}(t)$ which might partially cancel each other out. As the intensity of the applied laser field increases, it is apparent from the relationship between $E(t)$ and $j(t)$ that the polarization current will be converted into ionization current. The phase lag between them decreases, which is due to the occurrence of strong excitation and tunneling ionization mechanisms. Figures 11(a_2)–11(c_2), in the most intuitive way, show that the energy absorption is maximized when the electric current density is matched in phase to the electric field of ultrashort pulses and minimized when there is a phase difference of about $\pi/2$ between them, in line with the absorption energy formula mentioned earlier. The absorption energy at the end of the pulse laser is $E_{\rm abs}^{(a_2)} < E_{\rm abs}^{(b_2)} < E_{\rm abs}^{(c_2)}$. After the laser pulse is over, at the time of 120 a.u., the coherent oscillations on the field trailing edge still exist in the form of oscillations with much smaller amplitudes. The reason for this phenomenon is that a number of electrons are transferred into the conduction band, and a partial coherence between the involved nonstationary states is the characteristic of plasmonic metal systems, which is also referred to as dynamic metallization.

Figure 11(b) gives the electric conductivity $\sigma(\omega)$ of cBN corresponding to panel (a), where the $\sigma(\omega)$ of excited cBN may be extracted from the probe current density $j^{\rm probe}(t)$ by the equation

$$\sigma_{m,m}(\omega) = \frac{\int e^{i\omega t} j_m^{\rm probe}(t)dt}{\int e^{i\omega t} E_{{\rm eff},m}^{\rm probe}(t)dt}. \tag{10}$$

But in transverse geometry, the effective electric field $\mathbf{E}_{\rm eff}(t)$ does not include the induced field $\mathbf{E}_{\rm ind}(t)$; $\mathbf{E}_{\rm eff}(t) = \mathbf{E}_{\rm ext}(t)$. And $\sigma(\omega)$ is associated with the dielectric function by the formula [27] $\varepsilon_{m,m}(\omega) = 1 + i4\pi\sigma_{m,m}(\omega)/\omega$.

As plotted in Fig. 11(b), the magenta short dashed line denotes the real part of $\sigma(\omega)$ and the olive green short dotted line denotes the imaginary one. For the lower intensity of $I = 10^{13}$ W/cm^2, the $\sigma(\omega)$ of both real and imaginary parts in two geometries is consistent with that at the ground state marked with light gray solid line in Figs. 11(d_1) and 11(d_2). As the intensity of the laser increases, the $\sigma(\omega)$ in longitudinal geometry changes slowly, whereas the change in transverse geometry is clearly visible. It reflects that adding the metal electrode, i.e., the transverse geometry, is also an effective means to manipulation.

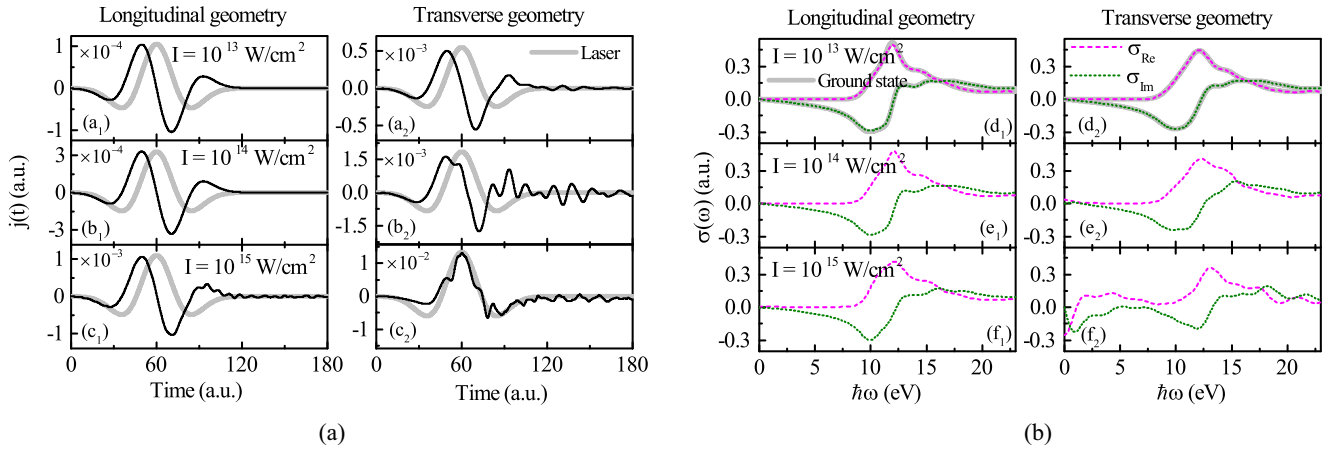

FIG. 11. (a) The calculated current density $j(t)$ in cBN induced by single-pulse laser as a function of the time evolution. The laser pulse is polarized along the x axis with a frequency of $\omega_l = 2.72$ eV ($\tau = 20$ a.u.), length of 6τ (120 a.u.), after which there is a field-free evolution of 3τ (60 a.u.). The varying peak laser intensities are from $I = 10^{13}$ W/cm^2 to $I = 10^{15}$ W/cm^2 both in the longitudinal geometry (left panel) and the transverse geometry (right panel). (b) The electric conductivity $\sigma(\omega)$ calculated in two geometries of cBN corresponding to the intensity of panel (a) after the laser irradiation.

IV. CONCLUSIONS

In summary, we investigate the transient dielectric response of cBN modulated by an ultrashort laser pulse within the framework of TDDFT. The main results of the study are as follows: (i) It would be achievable to control transient dielectric properties of cBN reversibly without physical damage via a shaped ultrashort laser field. (ii) For weaker laser fields $I < 5\times10^{14}$ W/cm^2, the excited cBN tends to be isotropic. As the laser field increases, the anisotropy of the dielectric function will be more pronounced until it exhibits hyperbolic dispersion. The position of the hyperbolic working frequency window could be controlled with some proper pulse parameters, such as intensity and duration or frequency. (iii) We clarified the evolution of the dielectric function at various time points during the pulse which exhibits reversible and damage-free modification in optical responses. (iv) The free relaxation time between the pump and probe laser field can be used for one of the effective manipulation parameters. (v) Adding metal electrodes to the system can significantly enhance the capability to control optical responses of dielectrics due to the suppression of the induced electric field in the transverse geometry. Looking to the future, it is interesting to note that shaped ultrashort intense laser pulses with a duration shorter than the dephasing time may be used as a tool to steer transient changes in the optical and electric properties of a medium over time intervals much shorter than a period of optical oscillations, preferably with high selectivity and high efficiency and without imposing physical damage, providing unique avenues for both basic research and applications, such as ultrafast nondestructive all-optical devices, coherent pulse reshaping, and a relatively unexplored regime of light-wave electronics [71]. Thus, this deserves to be investigated in future research both theoretically and experimentally.

ACKNOWLEDGMENTS

This work was supported by the National Key R&D Program of China (Grant No. 2018YFB1107200), the National Natural Science Foundation of China (Grants No. 11774030 and No. 51735001), and the Fundamental Research Funds for the Central Universities (Grant No. 2017CX10007).

[1] M. Durach, A. Rusina, M. F. Kling, and M. I. Stockman, Phys. Rev. Lett. **105**, 086803 (2010).
[2] M. Durach, A. Rusina, M. F. Kling, and M. I. Stockman, Phys. Rev. Lett. **107**, 086602 (2011).
[3] V. Apalkov and M. I. Stockman, Phys. Rev. B **86**, 165118 (2012).
[4] V. Apalkov and M. I. Stockman, Phys. Rev. B **88**, 245438 (2013).
[5] A. Schiffrin, T. Paasch-Colberg, N. Karpowicz, V. Apalkov, D. Gerster, S. Mühlbrandt, M. Korbman, J. Reichert, M. Schultze, S. Holzner, J. V. Barth, R. Kienberger, R. Ernstorfer, V. S. Yakovlev, M. I. Stockman, and F. Krausz, Nature (London) **493**, 70 (2013).
[6] M. Schultze, E. M. Bothschafter, A. Sommer, S. Holzner, W. Schweinberger, M. Fiess, M. Hofstetter, R. Kienberger, V. Apalkov, V. S. Yakovlev, M. I. Stockman, and F. Krausz, Nature (London) **493**, 75 (2013).
[7] G. Wachter, C. Lemell, J. Burgdörfer, S. A. Sato, X. M. Tong, and K. Yabana, Phys. Rev. Lett. **113**, 087401 (2014).
[8] O. Kwon, T. Paasch-Colberg, V. Apalkov, B.-K. Kim, J.-J. Kim, M. I. Stockman, and D. Kim, Sci. Rep. **6**, 21272 (2016).
[9] H. K. Kelardeh, M. I. Stockman, and V. Apalkov, IEEE Trans. Nanotechnol. **15**, 51 (2016).
[10] J. D. Lee, W. S. Yun, and N. Park, Phys. Rev. Lett. **116**, 057401 (2016).
[11] A. Sommer, E. M. Bothschafter, S. A. Sato, C. Jakubeit, T. Latka, O. Razskazovskaya, H. Fattahi, M. Jobst, W. Schweinberger, V. Shirvanyan, V. S. Yakovlev, R. Kienberger, K. Yabana, N. Karpowicz, M. Schultze, and F. Krausz, Nature (London) **534**, 86 (2016).
[12] X. Zhang, F. Wang, L. Jiang, and Y. Yao, Phys. Rev. B **95**, 184301 (2017).
[13] X. Zhang, F. Wang, F. Zhang, and Y. Yao, Phys. Rev. B **97**, 014310 (2018).
[14] *Synthesis and Properties of Boron Nitride*, edited by J. J. Pouch and S. A. Alteroviz (Trans Tech, Aedermannsdorf, Switzerland, 1990).
[15] O. Mishima, J. Tanaka, S. Yamaoka, and O. Fukunaga, Science **238**, 181 (1987).
[16] M. A. L. Marques, A. Castro, G. F. Bertsch, and A. Rubio, Comput. Phys. Commun. **151**, 60 (2003).
[17] A. Castro, H. Appel, M. Oliveira, C. A. Rozzi, X. Andrade, F. Lorenzen, M. A. L. Marques, E. K. U. Gross, and A. Rubio, Phys. Status Solidi B **243**, 2465 (2006).
[18] A. K. Dhara and S. K. Ghosh, Phys. Rev. A **35**, 442 (1987).
[19] S. K. Ghosh and A. K. Dhara, Phys. Rev. A **38**, 1149 (1988).
[20] N. Troullier and J. L. Martins, Phys. Rev. B **43**, 1993 (1991).
[21] F. Kootstra, P. L. de Boeij, and J. G. Snijders, J. Chem. Phys. **112**, 6517 (2000).
[22] N. T. Maitra, I. Souza, and K. Burke, Phys. Rev. B **68**, 045109 (2003).
[23] G. F. Bertsch, J.-I. Iwata, A. Rubio, and K. Yabana, Phys. Rev. B **62**, 7998 (2000).
[24] K. Yabana, T. Nakatsukasa, J. I. Iwata, and J. F. Bertsch, Phys. Status Solidi B **243**, 1121 (2006).
[25] T. Otobe, M. Yamagiwa, J. I. Iwata, K. Yabana, T. Nakatsukasa, and G. F. Bertsch, Phys. Rev. B **77**, 165104 (2008).
[26] K. Yabana, T. Sugiyama, Y. Shinohara, T. Otobe, and G. F. Bertsch, Phys. Rev. B **85**, 045134 (2012).
[27] S. A. Sato, K. Yabana, Y. Shinohara, T. Otobe, and G. F. Bertsch, Phys. Rev. B **89**, 064304 (2014).
[28] A. Castro, M. A. L. Marques, and A. Rubio, J. Chem. Phys. **121**, 3425 (2004).
[29] See http://elk.sourceforge.net.
[30] J. P. Perdew, K. Burke, and M. Ernzerhof, Phys. Rev. Lett. **77**, 3865 (1996).
[31] R. M. Chrenko, Solid State Commun. **14**, 511 (1974).
[32] V. A. Fomichev and M. A. Rumsh, J. Chem. Phys. **48**, 555 (1968).

[33] Y. N. Xu and W. Y. Ching, Phys. Rev. B **44**, 7787 (1991).

[34] A. Zaoui and F. E. Hassan, J. Phys.: Condens. Matter **13**, 253 (2001).

[35] K. T. Park, K. Terakura, and N. Hamada, J. Phys. C: Solid State Phys. **20**, 1241 (1987).

[36] A. Abdiche, H. Abid, R. Riane, and A. Bouaza, Acta Phys. Pol. A **117**, 921 (2010).

[37] K.-M. Lee, C. M. Kim, S. A. Sato, T. Otobe, Y. Shinohara, K. Yabana, and T. M. Jeong, J. Appl. Phys. **115**, 053519 (2014).

[38] W. A. Harrison, in *Electronic Structure and the Properties of Solids: The Physics of the Chemical Bond* (Dover, New York, 1989), p. 176.

[39] E. Goulielmakis, M. Schultze, M. Hofstetter, V. S. Yakovlev, and J. Gagnon, Science **320**, 1614 (2008).

[40] P. Földi, M. G. Benedict, and V. S. Yakovlev, New J. Phys. **15**, 063019 (2013).

[41] Y. Osaka, A. Chayahara, H. Yokohama, M. Okamoto, T. Hamada, T. Imura, and M. Fujisawa, in *Synthesis and Properties of Boron Nitride*, edited by J. J. Pouch and S. A. Alteroviz (Trans Tech, Aedermannsdorf, Switzerland, 1990), pp. 277–294.

[42] D. Sangalli, J. A. Berger, C. Attaccalite, M. Grüning, and P. Romaniello, Phys. Rev. B **95**, 155203 (2017).

[43] F. Calvayrac, P. G. Reinhard, E. Suraud, and C. A. Ullrich, Phys. Rep. **337**, 493 (2000).

[44] M. A. Marques and E. K. Gross, Annu. Rev. Phys. Chem. **55**, 427 (2004).

[45] J. P. Perdew and A. Zunger, Phys. Rev. B **23**, 5048 (1981).

[46] J. P. Perdew, A. Ruzsinszky, G. I. Csonka, and O. A. Vydrov, G. E. Scuseria, L. A. Constantin, X. Zhou, and K. Burke, Phys. Rev. Lett. **100**, 136406 (2008); **102**, 039902(E) (2009).

[47] E. Knittle, R. M. Wentzcovitch, R. Jeanloz, and M. L. Cohen, Nature (London) **337**, 349 (1989).

[48] M. I. Stockman, S. V. Faleev, and D. J. Bergman, Phys. Rev. Lett. **88**, 067402 (2002).

[49] M. I. Stockman and P. Hewageegana, Appl. Phys. A **89**, 247 (2007).

[50] S. K. Sundaram and E. Mazur, Nat. Mater. **1**, 217 (2002).

[51] L. V. Keldysh, Sov. Phys. JETP **20**, 1307 (1965).

[52] S. A. Sato, Y. Shinohara, T. Otobe, and K. Yabana, Phys. Rev. B **90**, 174303 (2014).

[53] D. Sangalli and A. Marini, Europhys. Lett. **110**, 47004 (2015).

[54] V. G. Veselago, Sov. Phys. Usp. **10**, 509 (1968).

[55] C. Luo, S. G. Johnson, J. D. Joannopoulos, and J. B. Pendry, Phys. Rev. B **68**, 045115 (2003).

[56] J. B. Pendry, Phys. Rev. Lett. **85**, 3966 (2000).

[57] Z. Liu, H. Lee, Y. Xiong, C. Sun, and X. Zhang, Science **315**, 1686 (2007).

[58] S. Dai, Q. Ma, T. Andersen, A. S. Mcleod, Z. Fei, M. K. Liu, M. Wagner, K. Watanabe, T. Taniguchi, M. Thiemens, F. Keilmann, P. Jarillo-Herrero, M. M. Fogler, and D. N. Basov, Nat. Commun. **6**, 6963 (2015).

[59] D. R. Smith and D. Schurig, Phys. Rev. Lett. **90**, 077405 (2003).

[60] A. Poddubny, I. Iorsh, P. Belov, and Y. Kivshar, Nat. Photon. **7**, 948 (2013).

[61] M. Y. Shalaginov, V. V. Vorobyov, J. Liu, M. Ferrera, A. V. Akimov, A. Lagutchev, A. N. Smolyaninov, V. V. Klimov, J. Irudayaraj, A. V. Kildishev, A. Boltasseva, and V. M. Shalaev, Laser Photon. Rev. **9**, 120 (2015).

[62] F. Liu, L. Xiao, Y. Ye, M. Wang, K. Cui, X. Feng, W. Zhang, and Y. Huang, Nat. Photon. **11**, 289 (2017).

[63] V. P. Drachev, V. A. Podolskiy, and A. V. Kildishev, Opt. Express **21**, 15048 (2013).

[64] J. Sun, N. M. Litchinitser, and J. Zhou, ACS Photon. **1**, 293 (2014).

[65] S. Guan, S. Y. Huang, Y. Yao, and S. A. Yang, Phys. Rev. B **95**, 165436 (2017).

[66] N. Miyata, K. Moriki, O. Mishima, M. Fujisawa, and T. Hattori, Phys. Rev. B **40**, 12028(R) (1989).

[67] G. Satta, G. Cappellini, V. Olevano, and L. Reining, Phys. Rev. B **70**, 195212 (2004).

[68] M. Esslinger, R. Vogelgesang, N. Talebi, W. Khunsin, P. Gehring, S. de Zuani, B. Gompf, and K. Kern, ACS Photon. **1**, 1285 (2014).

[69] D. M. Henderson, IEEE J. Quantum Electron. **18**, 921 (1982).

[70] M. A. Noginov, Y. A. Barnakov, G. Zhu, T. Tumkur, H. Li, and E. E. Narimanov, Appl. Phys. Lett. **94**, 151105 (2009).

[71] E. Goulielmakis, V. S. Yakovlev, A. L. Cavalieri, M. Uiberacker, V. Pervak, A. Apolonski, R. Kienberger, U. Kleineberg, and F. Krausz, Science **317**, 769 (2007).